

## RESEARCH ARTICLE

# Deciphering Augmented Dual-ROS-Driven Biofilm Eradication by Facilitating Long-Range Spatial Charge Decoupling in Polymer Carbon Dots

 Shujing Wang<sup>1</sup> | Lei Rong<sup>1</sup> | Yanbai Chen<sup>1</sup> | Wenxuan He<sup>1</sup> | Xiang Wen<sup>2</sup> | Yi Deng<sup>1</sup>  | Shuangquan Lai<sup>1</sup> 
<sup>1</sup>School of Chemical Engineering, Sichuan University, Chengdu, China | <sup>2</sup>Department of Dermatology, West China Hospital, Sichuan University, Chengdu, China

**Correspondence:** Yi Deng ([dengyibandeng@scu.edu.cn](mailto:dengyibandeng@scu.edu.cn)) | Shuangquan Lai ([shuangquanlai@scu.edu.cn](mailto:shuangquanlai@scu.edu.cn))

**Received:** 2 April 2026 | **Revised:** 12 May 2026 | **Accepted:** 18 May 2026

**Keywords:** biofilm eradication | donor-acceptor architecture | dual reactive oxygen species | polymer carbon dots | spatial charge decoupling

## ABSTRACT

Developing carbon dots (CDs) with reactive oxygen species (ROS) production capability provides an attractive approach to address the dilemma of biofilm eradication caused by the robust extracellular polymeric substance (EPS) matrix. The challenge for the exploration of highly potent CDs is to circumvent the severe thermodynamic and kinetic paradox to transform surrounding substrates into ultra-reactive ROS. To address this conundrum, we propose a long-pathway electron-accepting strategy promoting the absolute spatial charge decoupling by the elaborate marriage of carbonized core and polynaphthalenediimide (PNDI) network, which significantly boosts the superoxide anion ( $\cdot\text{O}_2^-$ ) and hydroxyl radical ( $\cdot\text{OH}$ ) dual-ROS generation of the constructed polymer CDs. Systematic mechanism exploration reveals that ultrafast intramolecular charge transfer after photoirradiation enables energetic long-life electrons to migrate along the PNDI highway for abundant  $\cdot\text{O}_2^-$  production. Intriguingly, this profound separation firmly anchors uncompensated highly oxidative holes at the extraordinarily deep highest occupied molecular orbital level of the carbon core, successfully unlocking the thermodynamic threshold for direct  $\cdot\text{OH}$  generation. This tailored dual-ROS storm induces catastrophic EPS matrix degradation and massacres the embedded pathogens, achieving near-complete ( $\sim 99.9\%$ ) eradication of *Escherichia coli* and *Staphylococcus aureus* biofilms. This work establishes a potent nanoplatform and provides profound mechanistic insights for tackling global biofilm-associated threats.

## 1 | Introduction

Microbial biofilms, as well-tolerated and ubiquitous biological architectures, have attracted wide attention for posing profound systemic threats across clinical medicine [1, 2], environmental engineering, [3, 4] and global infrastructure [5, 6]. In environmental and industrial contexts, biofilms drive detrimental biofouling, biocorrosion, and severe system blockages, while in clinical settings, they orchestrate antimicrobial resistance and evade host immune responses, precipitating persistent chronic infections and the catastrophic failure of medical implants [6,

7]. Collectively, these resilient microbial communities trigger immense global crises, inflicting nearly USD 4 trillion in annual global economic losses [8]. Crucially, the extreme recalcitrance of biofilms stems not merely from the embedded pathogens, but fundamentally from the robust extracellular polymeric substance (EPS) matrix, which is primarily composed of extracellular DNA (eDNA), polysaccharides, and proteins [9]. Contemporary consensus dictates that merely killing bacteria without thoroughly dismantling the EPS network yields only transient success, as the residual EPS matrix inevitably acts as a scaffold for rapid recolonization [10, 11]. Consequently, developing advanced

strategies capable of fundamentally disintegrating the complex EPS matrix while subsequently eliminating the embedded pathogens remains an urgent, yet unresolved, global imperative.

Lately, an attractive approach to surmount the obstacle of biofilm recalcitrance is to utilize carbon dots (CDs) as next-generation nanophotosensitizers to trigger reactive oxygen species (ROS) [12–14]. However, the development of highly potent CDs faces a severe thermodynamic and kinetic paradox. To achieve broad-spectrum light harvesting, conventional strategies often rely on constructing highly rigid and extended conjugated domains. While this successfully narrows the bandgap, it inherently compromises the redox potential and exacerbates the ultrafast radiative recombination of photogenerated electron-hole pairs due to highly overlapped wavefunctions [15, 16]. Consequently, these systems are typically restricted to generating mild, single-type ROS, such as singlet oxygen ( $^1\text{O}_2$ ) or superoxide radicals ( $\cdot\text{O}_2^-$ ) [17]. Among the ROS, hydroxyl radical ( $\cdot\text{OH}$ ), with its exceptionally high oxidation potential, is recognized as the most aggressive species that could react with virtually all biological molecules within the robust EPS matrix, including DNA, carbohydrates, and proteins [18–21]. Therefore, relying solely on the generation of mild ROS like  $^1\text{O}_2$  or  $\cdot\text{O}_2^-$  is kinetically inadequate to dismantle the robust EPS components. To retrofit the molecular design, constructing donor-acceptor (D-A) structures within CDs has been identified as an effective paradigm to suppress photoinduced charge recombination, but current designs predominantly rely on grafting discrete small-molecule electron acceptors onto the carbon core, meaning that photogenerated electrons can only migrate to the adjacent interface region [22]. In such localized systems, the short exciton diffusion length and persistent Coulombic attraction inevitably lead to rapid back-electron transfer, precluding the system from sustaining the highly oxidative holes at the deep highest occupied molecular orbital (HOMO) required to drive kinetically sluggish water oxidation for  $\cdot\text{OH}$  generation. Accordingly, a sophisticated strategy that transcends discrete molecules by constructing a continuous, long-pathway electron-accepting polymer network crosslinked in situ with the carbon core, enabling long-range spatial charge decoupling for a synergistic dual-ROS storm, is critically required.

Driven by these considerations, here we propose a continuous long-pathway electron-accepting strategy promoting the long-range spatial charge decoupling of electron-hole pairs by the elaborate marriage of in situ carbonized cores and crosslinked polynaphthalenediimide (PNDI) networks, which significantly boosts the synergistic dual-ROS generation (Scheme 1a). The resultant red-emissive polymer CDs (R-PCDs), featuring a bespoke alternating D-A-D-A architecture, are tailored via in situ solvothermal polymerization of 1,4,5,8-naphthalenetetracarboxylic dianhydride (NTCDA) and *o*-phenylenediamine (*o*-PDA) (Scheme 1b). Different from reported localized D-A systems, systematic mechanism exploration reveals that ultrafast intramolecular charge transfer (ICT) after photoirradiation pumps high-energy electrons from the carbon core into the strongly electron-withdrawing PNDI transport highway (Scheme 1c). This continuous polymeric pathway ensures electrons are transported far from the core, spatially localizing them in the peripheral molecular state to generate a substantial amount of  $\cdot\text{O}_2^-$ . Crucially, this profound spatial separation firmly anchors uncompensated, highly oxidative holes

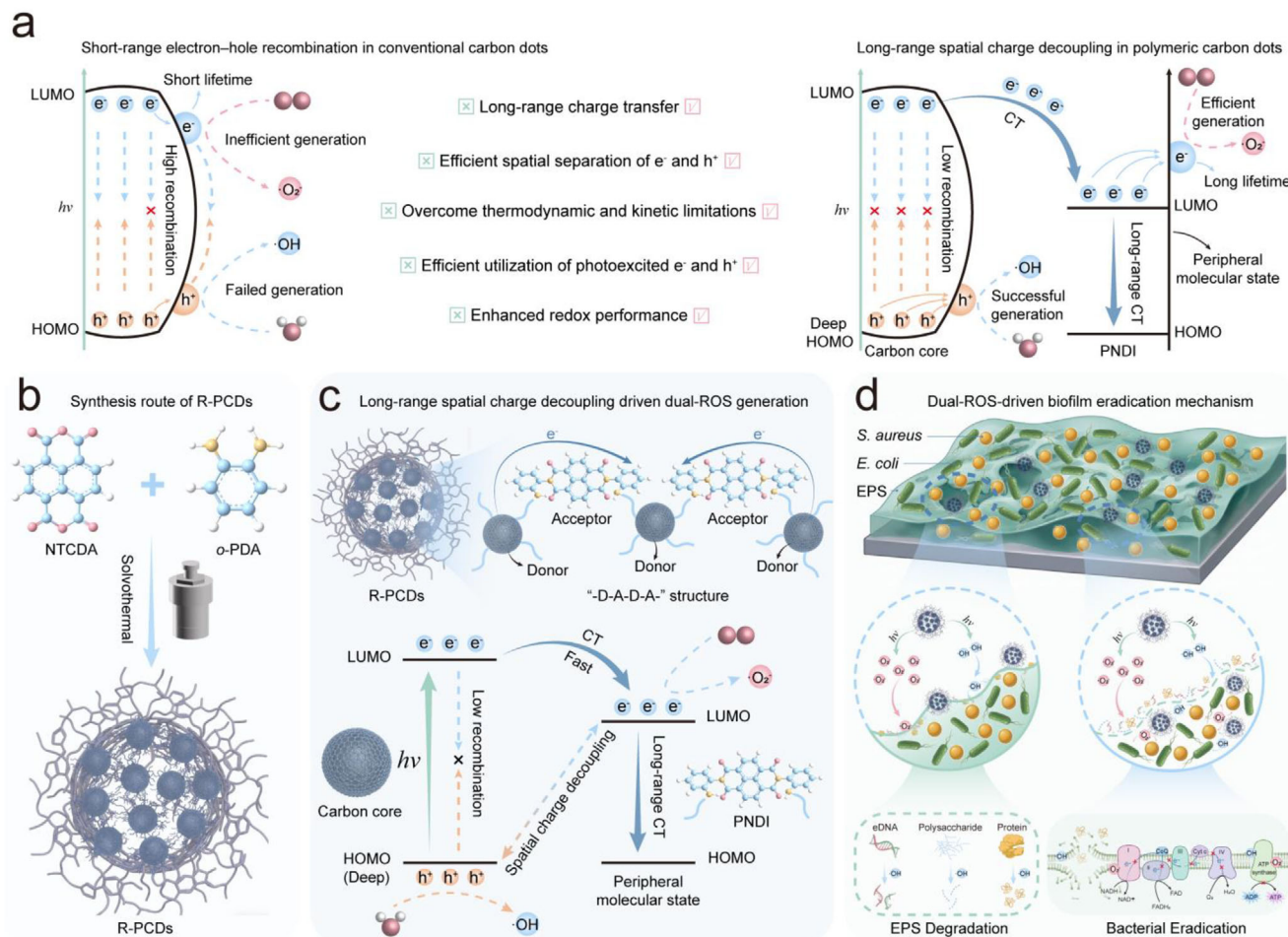
within the extraordinarily deep HOMO of the carbon core, successfully unlocking the stringent thermodynamic requirements for direct  $\cdot\text{OH}$  generation. By complementing the catastrophic degradation of eDNA, polysaccharides, and proteins within the EPS matrix with the lethal membrane disruption, blockade of respiratory chains, and rapid adenosine triphosphate (ATP) depletion of exposed bacteria, this as-prepared nanoplatfrom exhibits fabulous photocytotoxicity, achieving near-complete eradication of recalcitrant *Escherichia coli* (*E. coli*) and *Staphylococcus aureus* (*S. aureus*) biofilms (Scheme 1d). This study provides profound photophysical insights into long-range spatial charge decoupling in D-A structured nanomaterials and establishes a versatile and highly potent nanoplatfrom for combating global biofilm threats across biomedical, environmental and industrial applications.

## 2 | Results and Discussion

### 2.1 | Synthesis and Characterization of CDs

In this study, self-polymerized red-emissive CDs featuring a bespoke alternating D-A-D-A architecture were synthesized via a facile one-step solvothermal approach using NTCDA and *o*-PDA as precursors (Figures S1–S3). This distinctive photoluminescence (PL) behavior is likely ascribed to the extensive cross-linking of polymer chains on the CDs' surfaces [23]. To verify the successful synthesis, the morphology and microstructure of the as-prepared R-PCDs were initially investigated using transmission electron microscopy (TEM). As depicted in Figures 1a,b, the R-PCDs exhibit a pronounced cross-linked polymeric network morphology with a surprisingly large average size of  $54.2 \pm 0.7$  nm. Compared to conventional isolated small-molecule CDs, this significantly expanded dimension provides direct morphological evidence for the formation of an extended, continuous polymer network that cross-links multiple carbon cores, establishing the physical foundation for a long charge-migration pathway. High-resolution TEM (HRTEM) reveals well-defined lattice fringes with an interplanar spacing of 0.21 nm, corresponding to the (100) facet of graphitic carbon (Figure 1c) [24]. This highly crystallized  $\text{sp}^2$  carbon core lays a solid structural foundation for the intrinsic state of the electron-donating units [25], and fast Fourier transform (FFT) analysis further confirms the amorphous, non-crystalline structure of the PNDI polymer network surrounding the carbon core (Figure S4). The X-ray diffraction (XRD) pattern (Figure 1d) further corroborates the composite structure of R-PCDs, which comprises both carbon domains and polymeric molecular components, exhibiting a dominant diffraction peak at  $2\theta = 25.2^\circ$  assigned to the (002) plane of the graphitic structure [26]. Additionally, numerous sharp diffraction peaks are present, resembling the characteristic peaks of previously reported carbonized polymer dots containing polymeric structures [23].

To elucidate the chemical composition and surface functionalities, which are crucial for the formation of deep defective, surface, and molecular states [27], Fourier transform infrared (FTIR) spectroscopy and X-ray photoelectron spectroscopy (XPS) were performed. Compared to the FTIR spectrum of the precursor *o*-PDA (Figure 1e), the characteristic absorption peaks at  $3382\text{ cm}^{-1}$  and  $3358\text{ cm}^{-1}$ , arising from N-H stretching vibrations, are absent in the spectrum of R-PCDs [28]. Concurrently, the



**SCHEME 1** | (a) Comparative schematic diagram of short-range electron-hole recombination in conventional carbon dots versus long-range spatial charge decoupling in polymeric carbon dots for  $\cdot\text{O}_2^-$  and  $\cdot\text{OH}$  generation. (b) Schematic diagram of the synthesis of R-PCDs. (c) Schematic illustration of the “D-A-D-A” structure, spatial charge decoupling, and long-range charge transfer mechanism of R-PCDs. (d) Schematic illustration of the dual-ROS-driven biofilm eradication mechanism of R-PCDs.

C = O stretching vibration peak of NTCDA at approximately  $1760\text{ cm}^{-1}$  disappears, accompanied by the emergence of a new O = C-N stretching vibration peak at around  $1687\text{ cm}^{-1}$  in R-PCDs [29]. Furthermore, the peaks observed at  $1381\text{ cm}^{-1}$  and  $1132\text{ cm}^{-1}$  correspond to the asymmetric and symmetric stretching vibrations of C-N-C, respectively. These results collectively indicate the successful successive polycondensation of NTCDA and *o*-PDA, leading to the formation of an extended PNDI network within R-PCDs. Rather than acting as discrete molecular acceptors, this continuous PNDI structure serves as a strongly electron-withdrawing, long-pathway acceptor matrix grafted around the carbon cores. Moreover, XPS was employed to analyze the elemental composition and valence states of the R-PCDs. The XPS survey spectrum (Figure 1f) confirms the presence of C (80.68%), N (11.78%), and O (7.54%). In the C 1s spectrum (Figure 1g), the peaks can be deconvoluted into C-C/C = C (284.2 eV), C-N (284.9 eV), C-O (285.3 eV), C = N (286.5 eV), C = O (288.1 eV), and a  $\pi-\pi^*$  satellite peak (290.8 eV). The N 1s spectrum (Figure 1h) reveals peaks corresponding to pyridinic N (398.4 eV), pyrrolic N (400.3 eV), and graphitic N (400.8 eV), which introduce abundant deep defective and surface states. Notably, the specific peak at 399.1 eV, assigned to imide nitrogen (O = C-N-C = O), further substantiates the robust covalent integration of the continuous

PNDI acceptor network [30]. The O 1s spectrum (Figure 1i) similarly displays characteristic deconvoluted peaks for C = O (531.4 eV), C-O (532.3 eV), and -COOH (537.6 eV). Furthermore, the surface charge properties of R-PCDs were evaluated via Zeta potential measurements. Owing to the abundance of C = O groups, the R-PCDs exhibit a negative Zeta potential of -5.08 mV at pH = 7.0. Under acidic conditions (pH = 5.0), this negative value decreases to -3.87 mV due to the protonation of surface groups. Conversely, in an alkaline environment (pH = 9.0), the potential becomes even more negative (-6.97 mV) as the functional groups undergo further deprotonation (Figure S5). This pH-responsive charge behavior strongly corroborates the FTIR and XPS results, confirming the presence of numerous ionizable oxygen- and nitrogen-containing functional groups (e.g., -COOH, as well as pyridinic N and pyrrolic N) on the surface of R-PCDs. These functional groups not only ensure the excellent aqueous dispersibility of R-PCDs but also constitute the critical deep defective and surface states that facilitate cascaded electron transfer, while ensuring the highly oxidative photogenerated holes are securely anchored within the intrinsic states of the highly crystallized graphitic core. Thermogravimetric analysis (TGA) and nuclear magnetic resonance (NMR) spectroscopy confirm the polymeric structure of the R-PCDs



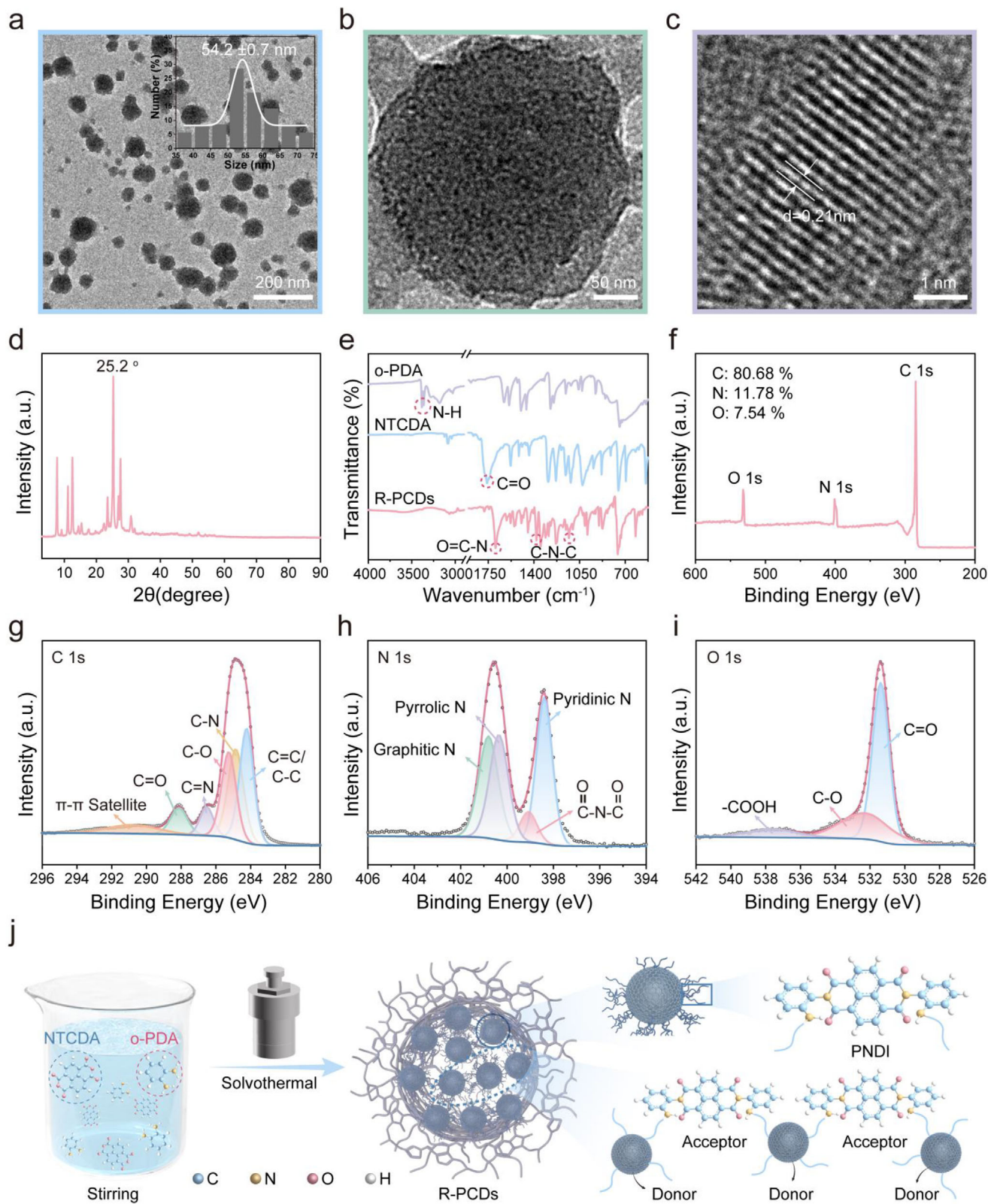


**FIGURE 1** | Synthesis and characterization of R-PCDs. (a, b) TEM and (c) HRTEM images of R-PCDs. (d) XRD pattern of R-PCDs. (e) FTIR spectra of NTCDA, o-PDA, and R-PCDs. (f) XPS survey spectrum, and (g) C 1s, (h) N 1s, and (i) O 1s spectra of R-PCDs. (j) Schematic illustration of the synthetic pathways and structure of R-PCDs.

(Figures S6, S7). These structural characterizations compellingly demonstrate that R-PCDs possess a unique alternating D-A architecture (Figure 1j). Within this architecture, the electron-rich graphitic cores (donors) are covalently intertwined with the extended, electron-withdrawing PNDI networks (acceptors). This continuous polymeric matrix not only prevents the aggregation-induced quenching of the cores but, more importantly, constructs a long-range spatial pathway essential for genuine spatial charge decoupling and subsequent synergistic dual-ROS generation. Its unique structure and properties stand in stark contrast to those of carbon dots containing discrete molecular acceptors (D-CDs) (Figures S8–S10).

## 2.2 | Optical Properties and Charge Transfer of R-PCDs

To fundamentally elucidate the structure-property relationship and unique optical behavior of R-PCDs, we first propose a photoluminescence (PL) mechanism dominated by ICT to reveal their long-range charge transfer mechanism (Figure 2a). In R-PCDs, multiple emission centers exist, including the intrinsic state of the highly crystalline carbon core, deep defective state, and surface state. Importantly, the unique alternating D-A-D-A configuration, with the crosslinked PNDI network serving as a strong electron-withdrawing acceptor, introduces the “molecular state”. Upon photoexcitation, an ultrafast ICT process is triggered, driving high-energy electrons to migrate stepwise toward the peripheral electron-deficient molecular state. This cascaded charge transfer effectively establishes a long-range charge transfer pathway while altering the dominant radiative recombination center, fundamentally accounting for the red fluorescence emission of R-PCDs.

This multi-emission-center mechanism is first confirmed by steady-state optical characterization. As illustrated in Figure 2b, the ultraviolet-visible (UV-Vis) absorption spectrum of the aqueous R-PCDs solution exhibits broad absorption spanning the entire visible region. The absorption bands in the 230–280 nm range can be ascribed to the  $\pi \rightarrow \pi^*$  transitions of C=C and C=N bonds within the carbon core, while the bands located at 280–400 nm and 400–510 nm originate from the  $n \rightarrow \pi^*$  transitions associated with the covalent polymeric network and surface functional groups. This suggests the presence of diverse defect-related states in R-PCDs, which, according to their absorption wavelengths, are designated as the intrinsic state, deep defective state, and surface state, respectively [31, 32]. Notably, the R-PCDs display a broad absorption band in the 510–800 nm range. According to the literature, existing naphthalenediimide-based charge-transfer (NDI-CT) complexes typically exhibit a new absorption peak in the 400–700 nm region of the UV-Vis spectrum, namely the charge-transfer (CT) absorption band, due to their alternating D-A stacking arrangement [33, 34]. Therefore, it can be deduced that a molecular state, induced by CT, also exists within the R-PCDs.

To validate these conclusions, the photoluminescence (PL) properties of R-PCDs in deionized water were characterized. The excitation-emission matrix (EEM) spectrum (Figure 2c) reveals a maximum emission center at 620 nm, alongside robust PL characteristics excitable across nearly the entire spectral range. Furthermore, the PL emission spectra (Figure 2d) exhibit an

excitation-independent emission profile with a fixed peak at 620 nm, displaying pronounced red fluorescence under both ultraviolet and visible light irradiation. The photoluminescence excitation (PLE) spectrum of R-PCDs (Figure 2e) further corroborates that the fluorescence emission is jointly contributed by the intrinsic, deep defective, and surface states (with the peak of the deep defective state partially masked by the harmonic peak at 315 nm). Concurrently, NDI-CT complexes typically appear red, and their fluorescence emission peaks are notably red-shifted due to the CT state possessing a lower energy level than the localized excited state. The resulting fluorescent CT emission band predominantly falls within the 520–640 nm range, which is a hallmark of the formation of CT complexes [34, 35]. These findings are in excellent agreement with the red macroscopic appearance and optical characterization results of R-PCDs, signifying that the unique emission properties of R-PCDs originate from the photoinduced ICT occurring between the encapsulated inner CDs and the bridging polymeric moieties. Specifically, the uniformly dispersed inner CDs in R-PCDs act as electron donors, while the strong electron-withdrawing inductive and conjugative effects of the imide groups ( $-\text{CO}-\text{N}-\text{CO}-$ ) significantly lower the lowest unoccupied molecular orbital (LUMO) energy level of the system, thereby enhancing its electron-accepting capability [36, 37]. This facilitates the formation of a molecular polymer via alternating D-A-D-A stacking. Consequently, the broad excitation band spanning the 460–605 nm region in Figure 2e stems from the CT from the surface state to the molecular state. The ICT within R-PCDs shifts the dominant fluorescence emission of the solution from the surface state to the molecular state, ultimately resulting in the prominent red-shift of the emission peak.

To elucidate the thermodynamic basis underlying the photocatalytic generation of dual ROS by R-PCDs, we systematically investigated their energy band structure. Derived from the Tauc plot, the optical HOMO-LUMO energy gap of the R-PCDs is determined to be 2.07 eV (Figure S11). This relatively narrow bandgap primarily stems from the ICT between the carbon core and the acceptor network, a feature that endows the material with an exceptional broadband visible-light-harvesting capability and ensures the highly efficient generation of excitons upon photoexcitation [38, 39]. To unambiguously delineate the generation mechanisms of the distinct ROS, the thermodynamic behaviors of photogenerated holes and electrons were decoupled and investigated separately. Regarding the generation of  $\cdot\text{OH}$ , valence band X-ray photoelectron spectroscopy (VB-XPS) reveals an exceptionally deep HOMO energy level of 3.28 eV vs. NHE (equivalent to -7.72 eV versus the vacuum level, calculated according to the IUPAC standard (Figure S12) [40, 41]. This highly positive oxidation potential is substantially deeper than the thermodynamic threshold required for the direct oxidation of  $\text{H}_2\text{O}$  to generate  $\cdot\text{OH}$  (+2.80 V vs. NHE), thereby providing a robust thermodynamic driving force for the deep-lying holes within the CDs to directly oxidize chemisorbed  $\text{H}_2\text{O}$  [42]. Meanwhile, the Mott-Schottky results confirm that the apparent macroscopic VB of R-PCDs is +2.01 V, which is higher than that of D-CDs and meets the thermodynamic potential threshold (+1.99 V) for the direct oxidation of  $\text{OH}^-$  in  $\text{H}_2\text{O}$  by holes to generate  $\cdot\text{OH}$  (Figure S13). Conversely, the generation of superoxide anions ( $\cdot\text{O}_2^-$ ) is highly contingent upon the intrinsic D-A-D-A architecture within the CDs. Driven by the pronounced electron push-pull effect between the donor and acceptor units, the molecule exhibits a significantly

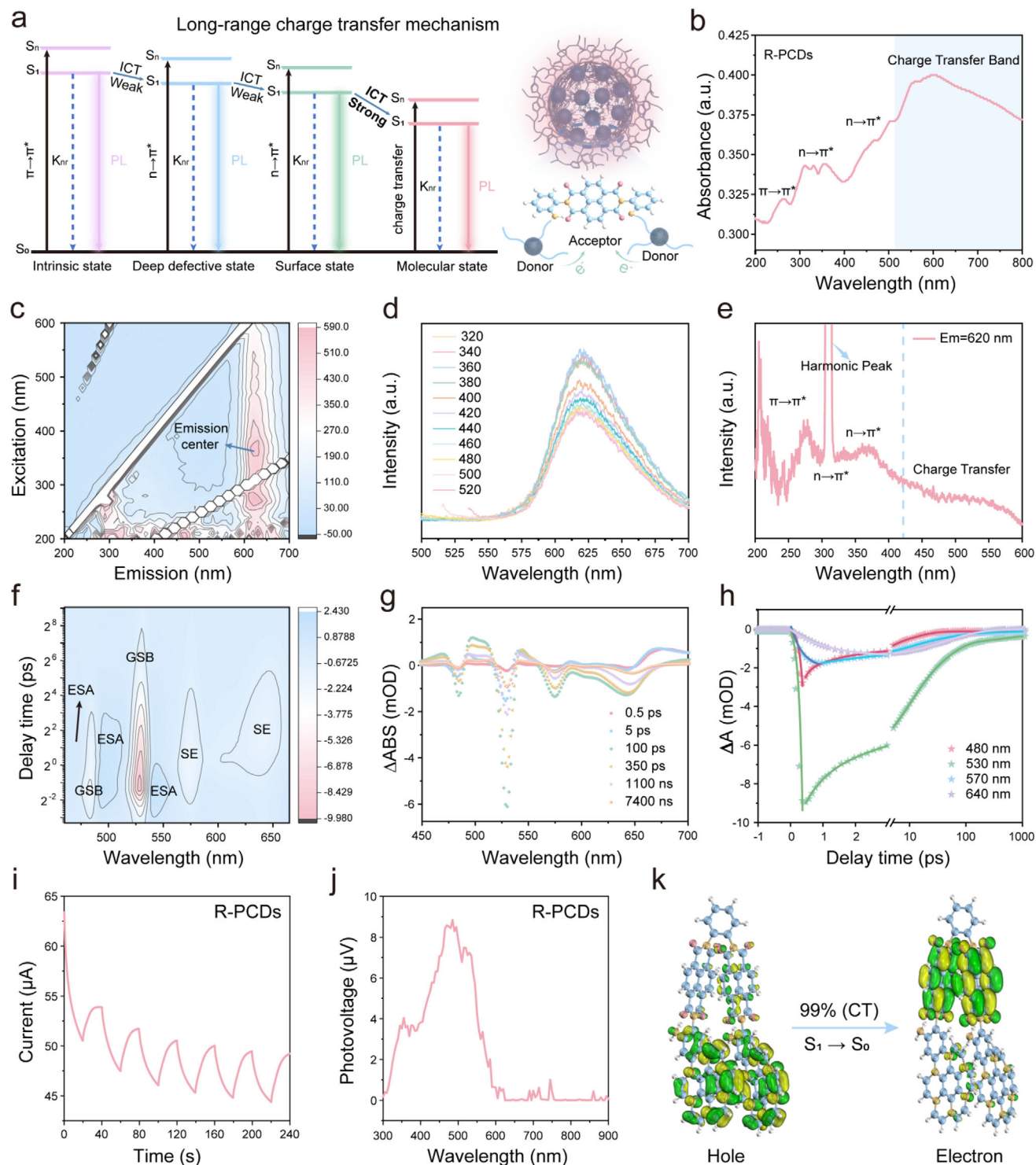


**FIGURE 2** | Photoluminescence and long-range spatial charge separation mechanisms of R-PCDs. (a) Schematic diagram of the photoluminescence and long-range charge transfer mechanisms of R-PCDs. (b) The absorption spectrum of R-PCDs in  $H_2O$ . (c) Excitation-emission map, (d) emission spectra under different excitation wavelengths, and (e) excitation spectrum at 510 nm emission wavelength for R-PCDs in  $H_2O$ . (f) Femtosecond broadband TA spectrum of R-PCDs under excitation of 365 nm. (g) TA spectra of R-PCDs at the different delay times. (h) Kinetic traces of R-PCDs at different probe wavelengths. (i) PC response curve and (j) SPV spectrum of R-PCDs under xenon lamp irradiation. (k) NTO patterns for the  $S_0 \rightarrow S_1$  transition of the simulated D-A-D fragment within R-PCDs.



enhanced charge separation efficiency. Precedent studies have demonstrated that the rational incorporation of appropriate D or A units can amplify the photogeneration capacity of  $\cdot\text{O}_2^-$  within D-A structured molecules [22, 43]. Specifically, upon photoexcitation, the formidable electron-withdrawing effect of the PNDI network enables photogenerated electrons to overcome Coulombic binding energy, driving their rapid transfer toward the peripheral acceptor molecular states. These highly energetic electrons, localized along the electron-deficient polymer chains, serve as optimal catalytic active sites for the single-electron reduction of dissolved  $\text{O}_2$ . This spatial decoupling of the strong oxidative power within the HOMO level and the high reductive activity at the molecular states lays a solid foundation for the synergistic generation of dual ROS.

Ultimately, to directly track the spatial charge separation mechanism on a temporal scale and unveil the genuine exciton dynamics, femtosecond transient absorption (fs-TA) spectroscopy measurements were performed on R-PCDs under 365 nm pulsed laser excitation. By monitoring the transient features at varying probe wavelengths, the carrier evolution processes across different emissive states can be intricately deciphered. Positive signals corresponding to excited-state absorption (ESA) are observed at 460 nm, 500 nm, and 540 nm. The negative signals emerging at 480 and 530 nm are assigned to the ground-state bleaching (GSB) of the surface states and molecular states, respectively. The latter exhibits significantly higher signal intensity and a prolonged delay time compared to the former, unequivocally indicating the occurrence of CT from the surface state to the molecular state. Stimulated emission (SE) signals of the surface and molecular states are detected at 570 and 640 nm, respectively (Figure 2f). However, the absence of a corresponding fluorescence emission peak at 570 nm in the emission spectrum of R-PCDs further corroborates the existence of an ICT process bridging the surface and molecular states. Furthermore, the comprehensive spectral evolution of R-PCDs across diverse delay times is delineated (Figure 2g). Concurrently, to elucidate the internal energy transfer pathways, carrier relaxation dynamics at disparate wavelengths were monitored, and the decay kinetic traces were fitted using a tri-exponential function. As illustrated in Figure 2h, the extracted carrier lifetimes ( $\tau_1$ ,  $\tau_2$ ,  $\tau_3$ ) and their respective fractional amplitudes (Table S3) offer conclusive kinetic evidence for this unique multi-level energy architecture.

Overall, a pronounced cascade-like prolongation in carrier lifetimes is observed as the probe wavelength red-shifts. At 480 nm, the kinetic decay is dominated by an ultrafast component,  $\tau_1$  (236.82 fs, 68.25%). This represents an ultrafast internal conversion and exciton dissociation process, characterized by the efficient dissociation of initial hot excitons and the subsequent rapid escape of photogenerated electrons from high-energy intrinsic states to lower energy levels [44, 45]. This ultrafast pump process not only initiates the subsequent directional CT but also effectively “isolates” the photogenerated holes possessing exceptional oxidative power (HOMO = 3.28 eV), anchoring them firmly within the graphitic core. Consequently, this provides ample kinetic preconditions for overcoming the high activation energy barrier necessary to directly oxidize  $\text{H}_2\text{O}$  into  $\cdot\text{OH}$ . As charges migrate peripherally, the lifetimes at 530 and 570 nm begin to exhibit a substantial increase. It is noteworthy that between 570 nm (surface state) and 640 nm (molecular state), the

intermediate-lifetime component  $\tau_2$ , which characterizes exciton dissociation and directional transfer, exhibits a significant jump, increasing sharply from 34.09 ps for the surface state to 104.57 ps for the molecular state. This dramatic surge compellingly substantiates that the formidable electron-withdrawing effect of the PNDI network induces a massive localized dipole moment [46, 47]. Compelled by this potent driving force, electrons accumulated at the surface state can effortlessly surmount the exciton binding energy, undergoing a strong CT toward the electron-deficient polymeric acceptor chains (molecular state). Unlike discrete small-molecule acceptors, this extended PNDI network provides a continuous, long-distance migration pathway for the electrons. Such long-range ICT profoundly suppresses back-electron transfer while precisely localizing highly active reductive electrons onto the outermost catalytic active sites [48]. The ultimate consequence of this cascade transfer pathway is the establishment of a long-lived charge-separated state. At 640 nm, an exceptionally prolonged lifetime component ( $\tau_3$ ) of 918.37 ps is observed, which strongly couples with the long-lived characteristics of the surface state (906.19 ps). Although the macroscopic apparent LUMO energy level of the system seems insufficient to wholly bridge the conventional reduction potential for  $\cdot\text{O}_2^-$ , the ultrafast ICT process effectively pumps unrelaxed, high-energy electrons into the peripheral electron-deficient polymer chains. Coupled with the massive localized charge polarization that favorably shifts the local thermodynamic microenvironment, these localized energetic electrons possess both the requisite thermodynamic driving force and ultra-long survival times to execute the single-electron reduction of dissolved  $\text{O}_2$  [49, 50]. In contrast, the final delay time of D-CDs is significantly shorter, indicating rapid electron-hole recombination (Figure S14, Table S2), whereas R-PCDs achieve spatially decoupled long-range electron transfer through the crosslinked polymeric electron acceptors and the D-A-D-A structure. Furthermore, R-PCDs exhibited a stable, strong, and reproducible photocurrent (PC) response under xenon lamp irradiation, significantly outperforming D-CDs, indicating the high charge separation efficiency (Figure 2i, S15) [51]. Meanwhile, the surface photovoltage (SPV) of R-PCDs reached 8.84  $\mu\text{V}$ , which is 9.3 times that of D-CDs, enabling exceptionally efficient spatial charge decoupling and long-range migration (Figure 2j, S16) [52]. Electrochemical impedance spectroscopy (EIS) and Hall effect measurements revealed that R-PCDs exhibit significantly lower charge transfer resistance, enhanced carrier mobility [48], and a substantially higher carrier concentration compared to D-CDs (Figure S17, 18). Finally, natural transition orbital (NTO) calculations of the emissive singlet state ( $\text{S}_1 \rightarrow \text{S}_0$ ) intuitively reveal that the  $\text{S}_1$  state of the simulated D-A-D fragment within R-PCDs exhibits 99% separation between holes and electrons, demonstrating a pronounced CT character (Figure 2k) [53].

### 2.3 | Evaluation of Reactive Oxygen Species (ROS) Generation and Kinetics

Based on the spatial decoupling CT dynamics elucidated above, we propose a mechanism for the generation of dual-ROS by R-PCDs under white light irradiation (Figure 3a). Specifically, strongly oxidizing holes firmly anchored in the deep HOMO of the carbon core directly oxidize  $\text{H}_2\text{O}$  to generate  $\cdot\text{OH}$ . Meanwhile, high-energy electrons pumped to the peripheral electron-deficient PNDI network via ultrafast ICT efficiently perform

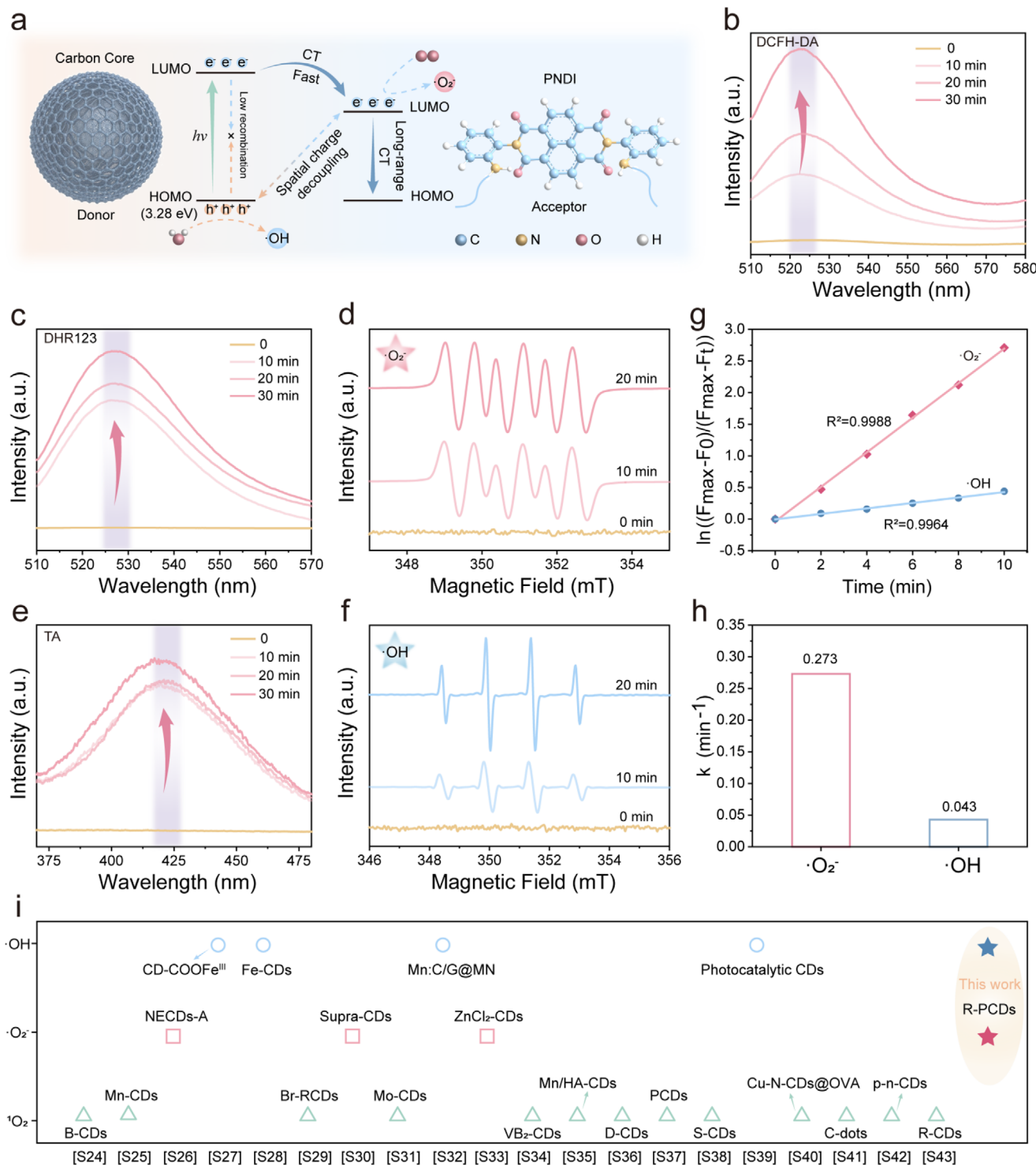


**FIGURE 3** | ROS generation and kinetic analysis of R-PCDs. (a) Schematic illustration of the mechanism for dual ROS ( $\cdot\text{O}_2^-$  and  $\cdot\text{OH}$ ) generation driven by long-range charge transfer and spatial charge decoupling within R-PCDs under light excitation. (b) Time-dependent fluorescence spectra of the DCFH-DA probe for monitoring total ROS generation. Time-dependent fluorescence spectra of (c) the DHR123 probe for  $\cdot\text{O}_2^-$  detection and (e) the TA probe for  $\cdot\text{OH}$  detection. ESR spectra of (d) DMPO- $\cdot\text{O}_2^-$  and (f) DMPO- $\cdot\text{OH}$  adducts under dark conditions and various irradiation times. (g) Pseudo-first-order kinetic fitting curves for the generation of  $\cdot\text{O}_2^-$  and  $\cdot\text{OH}$  based on the fluorescence data. (h) Comparison of the apparent reaction rate constants ( $k$ ) for  $\cdot\text{O}_2^-$  and  $\cdot\text{OH}$  generation catalyzed by R-PCDs. (i) Schematic diagram comparing CDs that generate only a single type of ROS with R-PCDs capable of releasing dual ROS.



single-electron reduction of dissolved  $O_2$ , generating substantial amounts of  $\cdot O_2^-$ .

To systematically evaluate the photocatalytic activity of the synthesized R-PCDs, their capacity for ROS generation under white light irradiation was investigated utilizing specific fluorescent probes and electron spin resonance (ESR) spectroscopy. Initially, the overall ROS production was monitored using the 2',7'-dichlorofluorescein diacetate (DCFH-DA) probe [54]. As illustrated in Figure 3b, prolonging the irradiation time from 0 to 30 min triggered a continuous and pronounced enhancement in the fluorescence emission intensity at 525 nm. Subsequent quantitative analysis revealed that after 30 min of irradiation, the relative fluorescence intensity ratio ( $I/I_0$ ) at 525 nm exhibited an approximately 280-fold surge (Figure S19a), providing compelling evidence for the robust overall ROS-generating capability of the R-PCDs. To further delineate the specific ROS components, dihydrorhodamine 123 (DHR123) and terephthalic acid (TA) were employed as selective probes for detecting  $\cdot O_2^-$  and  $\cdot OH$ , respectively [54, 55]. Figure 3c demonstrates a steady and continuous time-dependent intensification of the characteristic fluorescence peak of oxidized DHR123 at 528 nm, corroborating the continuous evolution of  $\cdot O_2^-$ . Concurrently, the TA fluorescence spectra (Figure 3e) exhibited a gradually amplifying emission peak at 425 nm. This is assigned to the formation of highly fluorescent 2-hydroxyterephthalic acid (hTA) via the reaction between TA and the endogenously generated  $\cdot OH$  [56]. Notably, a comparison of their relative fluorescence intensities pre- and post-irradiation revealed that after 30 min of light exposure, the  $I/I_0$  of the  $\cdot O_2^-$  probe surged by approximately 260-fold (Figure S19b). In contrast, the  $I/I_0$  of the  $\cdot OH$  probe increased by only about 135-fold, with its growth trajectory plateauing noticeably after 10 min (Figure S19c). This initial observation implies that  $\cdot O_2^-$  generation intrinsically dominates the photoexcitation process.

To unambiguously validate the evolution of these radical species, ESR spectroscopy was performed. The obtained ESR spectra displayed prominent, irradiation-time-dependent signal enhancements for both  $\cdot O_2^-$  (Figure 3d) and  $\cdot OH$  (Figure 3f). Remarkably, at 10 and 20 min of irradiation, the classic 1:2:2:1 quartet signal characteristic of the DMPO- $\cdot OH$  adduct and the typical multiplet signals of the DMPO- $\cdot O_2^-$  adduct were clearly resolved, respectively, perfectly corroborating the fluorescence probe findings. To quantitatively elucidate the underlying ROS generation dynamics, a chemical kinetic analysis was conducted on the fluorescence data (Figure S20a,b). The time-dependent evolution profiles of both  $\cdot O_2^-$  and  $\cdot OH$  exhibited excellent linear fits to a pseudo-first-order kinetic model (plotted as  $\ln((F_{\max}-F_0)/(F_{\max}-F_t))$  versus time), yielding exceptionally high correlation coefficients ( $R^2 = 0.9988$  and  $0.9964$ , respectively) (Figure 3g). As plotted in Figure 3h, the calculated apparent reaction rate constant ( $k$ ) for  $\cdot O_2^-$  generation reached  $0.273 \text{ min}^{-1}$ , which is approximately 6.3 times higher than that for  $\cdot OH$  generation ( $0.043 \text{ min}^{-1}$ ). This striking kinetic disparity unambiguously dictates that, although R-PCDs can actuate multiple radical generation pathways, the evolution of  $\cdot O_2^-$  constitutes the dominant photocatalytic mechanism. Furthermore, R-PCDs exhibit excellent photobleaching resistance, enabling them to maintain efficient ROS generation (Figure S21). As highlighted in Figure 3i, unlike CDs that can generate only a single type of ROS (Table S4), R-PCDs are capable of releasing highly destructive synergistic dual ROS, which

lays the foundation for their thorough degradation of the EPS matrix and eradication of bacteria within complex physiological microenvironments.

## 2.4 | Antibiofilm Properties of R-PCDs

Building upon the exceptional ROS-generating capacity of R-PCDs under white light irradiation, a robust physicochemical foundation is established for dismantling the formidable biofilm barrier and achieving highly efficient bactericidal outcomes. Consequently, we systematically evaluated their photodynamic bactericidal and biofilm eradication activities against typical Gram-negative (*E. coli*) and Gram-positive (*S. aureus*) bacteria. Initially, a standard spread-plate method was employed to visually assess the bactericidal efficacy of various treatments against biofilm-residing bacteria (Figure 4a). The results revealed dense colony growth for both *E. coli* and *S. aureus* in the untreated control group (Control), the white light alone group (WL), and the R-PCDs alone group in the dark. This observation dictates that white light alone lacks bactericidal capability, and R-PCDs exhibit excellent biocompatibility in the absence of photoexcitation. Strikingly, upon the synergistic application of R-PCDs and white light irradiation (R-PCDs+WL), scarcely any viable colonies were observed on the agar plates for either bacterial strain. Subsequent quantitative analysis (Figures 4b,c) demonstrated that the antibacterial rates of the R-PCDs+WL group against both *E. coli* and *S. aureus* soared to nearly 99.9%. This macroscopic outcome compellingly substantiates the potent photo-driven lethality of R-PCDs against deep-seated bacteria within biofilms. Beyond direct bacterial eradication, the deconstruction and clearance of the recalcitrant biofilm matrix, primarily composed of EPS, are pivotal for eradicating infections. Crystal violet (CV) staining was utilized to evaluate the total biofilm biomass across all groups. As depicted in the macroscopic photographs (Figure 4d), the wells of the three aforementioned control groups exhibited a deep purple hue, indicating the formation of dense and mature biofilms. In stark contrast, the purple color in the R-PCDs+WL group faded drastically, signifying the thorough disintegration of the biofilm architecture. Quantitative absorbance analysis (Figures 4e,f) further confirmed that following photodynamic treatment, the residual biofilm biomass of both *E. coli* and *S. aureus* decreased sharply, fully demonstrating the capability of R-PCDs to effectively penetrate and disrupt the biofilm defense system.

To in situ investigate the biofilm disruption and bacterial viability at a three-dimensional (3D) spatial level, LIVE/DEAD bacterial dual-staining (SYTO 9 for live bacteria in green, PI for dead bacteria in red) was performed (Figure 4g). In the confocal laser scanning microscopy (CLSM) three-dimensional (3D) reconstructed images, the Control, R-PCDs, and WL groups all displayed thick, dense, and intense green fluorescent networks, indicating intact biofilm structures with extremely high bacterial viability. In sharp contrast, the R-PCDs+WL group not only exhibited a significantly reduced 3D structural thickness but also presented a field of view almost entirely dominated by bright red fluorescence, with the green fluorescence virtually abolished. This intuitively and strikingly visualizes that the massive ROS generated by R-PCDs can effectively penetrate the EPS barrier, triggering irreversible cell membrane damage and

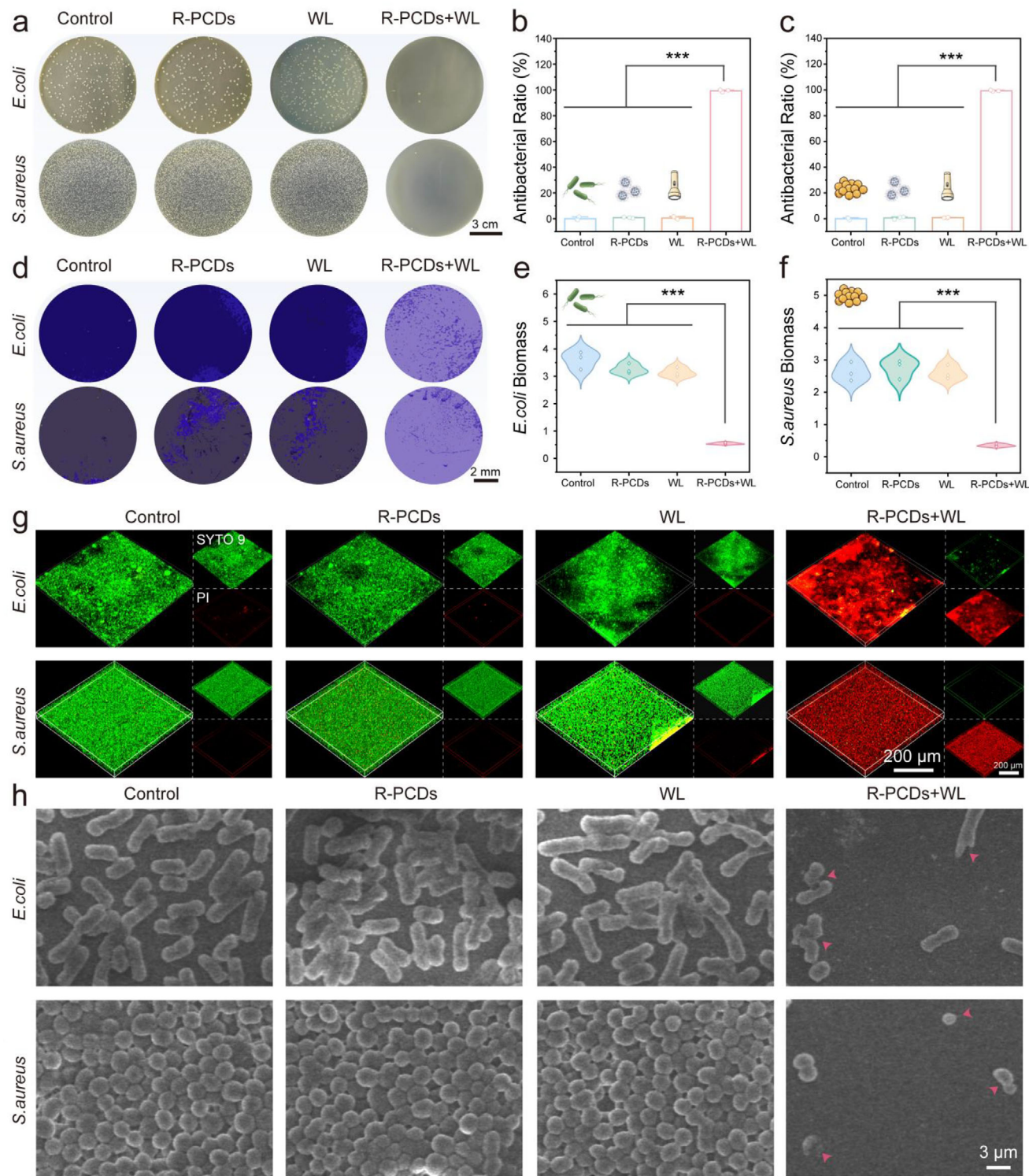


**FIGURE 4** | Anti-biofilm and photodynamic bactericidal activities of R-PCDs. (a) Photographs of agar plates showing the bactericidal efficacy against *E. coli* and *S. aureus* biofilms following various treatments (Control, R-PCDs, WL, and R-PCDs+WL). Corresponding quantitative antibacterial rates against (b) *E. coli* and (c) *S. aureus* biofilms. (d) Macroscopic images of biofilms stained with CV to evaluate total biomass. Quantitative analysis of the residual biofilm biomass based on CV absorbance for (e) *E. coli* and (f) *S. aureus*. (g) CLSM 3D reconstructed images of the biofilms after live/dead dual-staining (green: SYTO 9 for live bacteria; red: PI for dead bacteria). (h) SEM images reveal the morphological alterations and membrane damage of individual bacteria within the biofilms.  $n = 3$  for each group, \*\*\*:  $p < 0.001$ .

culminating in large-scale bacterial death within the biofilm. Finally, scanning electron microscopy (SEM) characterization was conducted to observe the morphological alterations of the biofilms and probe the eradication efficiency of different treatments (Figure 4h). In the three control groups, both *E. coli* (typical short rods) and *S. aureus* (typical spheres) presented smooth surfaces and plump morphologies, forming dense 3D architectures composed of intact, tightly adhered bacteria. Conversely, in the R-PCDs+WL group, the bacteria suffered devastating structural collapse (as indicated by the pink arrows): the dense biofilm was fragmented, and individual bacterial surfaces exhibited severe wrinkling and shrinkage. Pronounced membrane invagination and rupture occurred, and even substantial fragments of leaked intracellular contents from lysed bacteria were observed.

## 2.5 | Anti-biofilm Mechanism Decipherment

The aforementioned macroscopic and 3D in situ characterizations have conclusively corroborated the extraordinary biofilm eradication and bactericidal capabilities of R-PCDs under white light excitation. It is well established that the extreme recalcitrance of biofilms to conventional antimicrobial agents is primarily attributed to the abundant EPS matrix secreted by the resident bacteria. The EPS, predominantly interwoven with eDNA, polysaccharides, and proteins, constitutes a highly dense physical barrier that effectively impedes the penetration of external antimicrobial active species [57]. Therefore, we postulate that the crucial initial step underlying the superior photodynamic bactericidal efficacy of R-PCDs lies in the thorough deconstruction of the EPS matrix. To validate this hypothesis, specific fluorescent probes were employed to in situ stain and track the three core components of the biofilm. Initially, eDNA, which serves as a vital scaffold for maintaining the 3D structural integrity and stability of the biofilm, was visualized using SYBR Green staining (Figure 5a). In the Control, R-PCDs alone, and WL alone treatment groups, the biofilms of both *E. coli* and *S. aureus* exhibited extensive, dense, and continuous green fluorescence, indicating that their eDNA networks remained completely intact. However, upon the synergistic application of R-PCDs and white light (R-PCDs+WL), the green fluorescence signals within the field of view underwent a drastic attenuation and displayed a highly fragmented distribution. This visually substantiates that the photoexcited  $\cdot\text{O}_2^-$  and  $\cdot\text{OH}$  can effectively cleave the long chains of eDNA, dismantling its scaffolding function. Subsequently, the Calcofluor White M2R (CFW) probe was utilized to characterize  $\beta$ -polysaccharides, a pivotal component mediating initial bacterial adhesion and structural reinforcement (Figure 5b). In stark contrast to the dense and extensive blue fluorescent grids observed in the control groups, the blue fluorescence in the photodynamic treatment group (R-PCDs+WL) nearly vanished, leaving only a paucity of scattered spots, which unequivocally indicates that the polysaccharide matrix within the biofilm suffered severe oxidative degradation. Furthermore, a Sypro Orange probe was used to stain the extracellular protein macromolecules within the EPS (Figure 5c). Similarly, the intense oxidative stress induced by R-PCDs under irradiation led to the catastrophic disintegration and quenching of the originally uniform and robust yellow fluorescent network. Taken together, under the fierce onslaught of the high-concentration, strongly oxidative

$\cdot\text{O}_2^-$  and  $\cdot\text{OH}$  generated upon excitation, the biofilm architecture is thoroughly disrupted, directly leading to the complete exposure of the internally sheltered bacteria.

Deprived of the protective physical barrier afforded by the EPS, the bacteria are completely exposed to the hostile microenvironment, rendering their vital cell membranes the primary targets. To evaluate the extent of ROS-induced disruption to bacterial cell membrane integrity, we initially monitored the alterations in inner membrane permeability employing the *o*-nitrophenyl- $\beta$ -D-galactopyranoside (ONPG) hydrolysis assay (Figures 5d,e). ONPG itself is incapable of penetrating intact cell membranes; it can only enter the cytoplasm to be hydrolyzed into *o*-nitrophenol by  $\beta$ -galactosidase when membrane permeability increases. The results reveal that under treatments with either R-PCDs alone or WL alone, the ONPG hydrolysis rates in both *E. coli* and *S. aureus* systems remain negligible, showing no significant difference from the blank control group. However, upon the synergistic treatment of R-PCDs+WL, the ONPG hydrolysis levels in both bacterial strains exhibit a dramatic, stepwise escalation as the irradiation time extends from 10 to 30 min. This unequivocally demonstrates that the photoexcited  $\cdot\text{O}_2^-$  and  $\cdot\text{OH}$  trigger an irreversible and profound surge in membrane permeability. The disruption of the cell membrane is inevitably accompanied by a massive leakage of intracellular substances essential for sustaining life activities. We assayed the centrifuged supernatants utilizing a bicinchoninic acid (BCA) protein assay kit (Figures 5f,g). In high concordance with expectations, the concentration of soluble proteins in the supernatant of the photodynamic treatment group significantly ascends with prolonged irradiation time. After 30 min of irradiation, a substantial amount of proteins originally confined within the cells leak out, further corroborating the thorough disintegration and irreversible damage of the cell membrane architecture.

Concurrently, an iodinitrotetrazolium chloride (INT) reduction assay was conducted to quantitatively assess the electron transfer activity of dehydrogenases within the bacterial respiratory chain (Figures 5h,i). Under normal physiological states, metabolically active bacteria can reduce INT into a red formazan compound, which exhibits a strong absorption peak near 485 nm. As illustrated by the absorption spectra and the inset optical photographs, the control groups invariably present extremely high absorbance values and a deep red hue; nevertheless, under the sustained assault of R-PCDs+WL (10–30 min), the intensity of the absorption peak plummets dramatically, accompanied by a gradual fading of the solution's color. To furnish more precise statistical evidence, the absorbance values at 485 nm were extracted for quantitative comparison (Figure S22a,b). The results indicate that as the irradiation time is prolonged to 30 min, the absorbance of formazan in both *E. coli* and *S. aureus* systems experiences a highly significant and precipitous drop. This dual corroboration from both spectral and quantitative data visually reflects that the electron transfer process in the bacterial respiratory chain is forcibly blockaded, leading to the severe inhibition of metabolic enzyme activities. As the “energy currency” of the cell, the fluctuation in adenosine triphosphate (ATP) content directly dictates the life or death of the bacteria (Figures 5j,k). The data demonstrate that following photodynamic treatment, the intracellular ATP concentrations in both Gram-negative and Gram-positive bacteria undergo a cliff-like



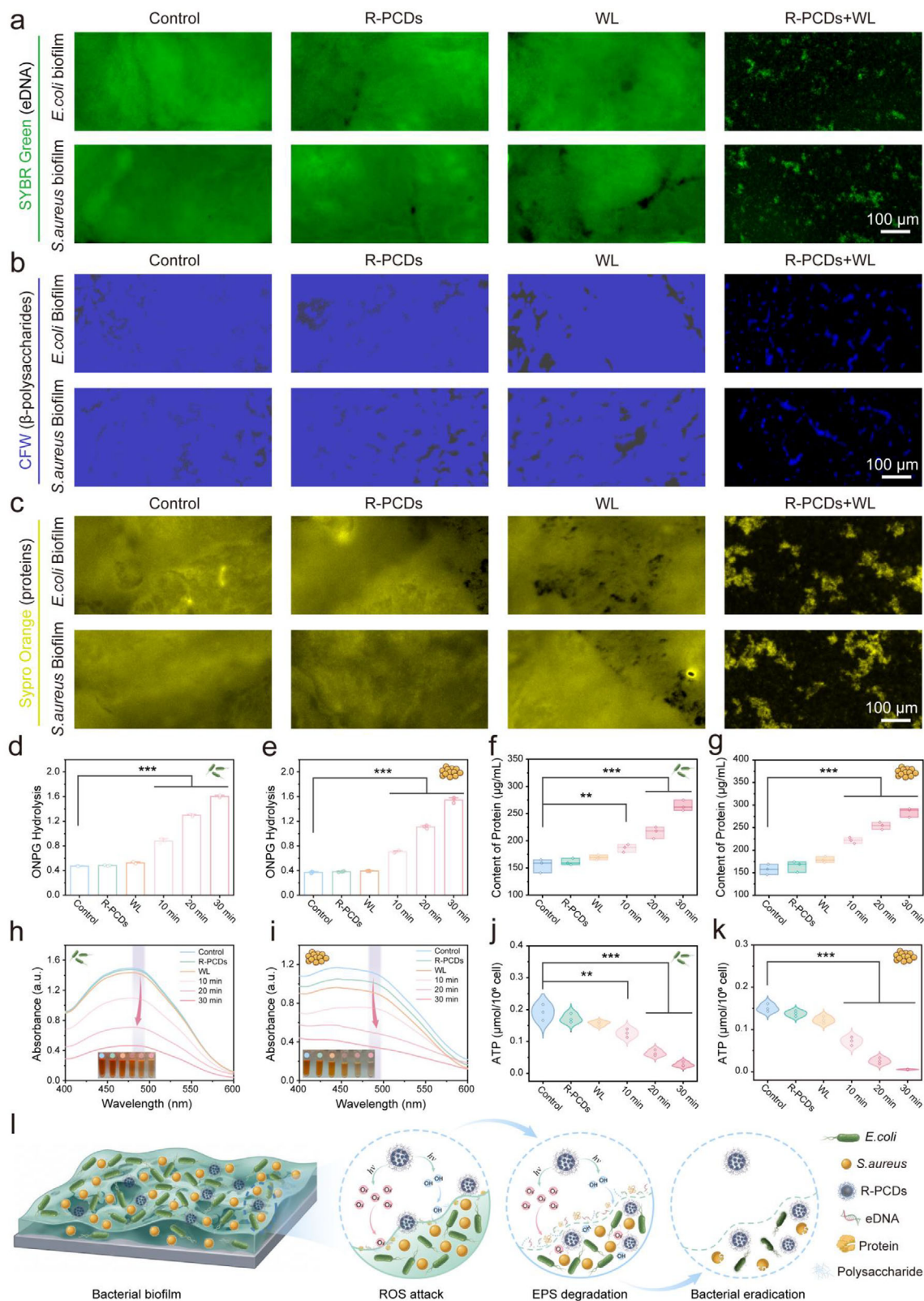


**FIGURE 5** | Elucidation of the anti-biofilm and antibacterial mechanisms of R-PCDs. Fluorescence images of *E. coli* and *S. aureus* biofilms stained with (a) SYBR Green for extracellular DNA (eDNA), (b) CFW for β-polysaccharides, and (c) Sypro Orange for extracellular proteins after diverse treatments. Inner membrane permeability assessed by the ONPG hydrolysis assay for (d) *E. coli* and (e) *S. aureus*. Quantitative analysis of intracellular protein leakage from (f) *E. coli* and (g) *S. aureus* utilizing the BCA assay. UV-vis absorption spectra and corresponding optical photographs (insets) from the INT reduction assay, evaluating the respiratory chain dehydrogenase activity of (h) *E. coli* and (i) *S. aureus*. Intracellular ATP concentrations of (j) *E. coli* and (k) *S. aureus* subjected to varied treatments (Control, R-PCDs, WL, and R-PCDs+WL for 10, 20, 30 min). (l) Schematic illustration elucidating the mechanism of R-PCDs-mediated photodynamic EPS matrix degradation and subsequent bacterial eradication. n = 3 for each group, \*\*:  $p < 0.01$ , \*\*\*:  $p < 0.001$ .

plunge. After 30 min of irradiation, ATP is virtually exhausted, declaring the total collapse of the bacterial energy metabolism system. TEM images of individual *E. coli* and *S. aureus* show obvious structural damage and leakage of cellular contents (Figure S23).

To intuitively summarize the above experimental findings, Figure 5l presents a panoramic model of the bactericidal mechanism. Upon white light excitation, the potent dual-ROS generated by R-PCDs first degrade the protective EPS matrix. Subsequently, they vigorously attack the underlying bacteria. From irreversible cell membrane disruption and substantial leakage of intracellular contents to respiratory chain paralysis and complete ATP depletion, the bacterial biofilm is ultimately eradicated thoroughly and irreversibly.

### 3 | Conclusion

In summary, we have successfully developed R-PCDs with a robust alternating D-A-D-A architecture, effectively overcoming the conventional trade-off between broadband light harvesting and redox driving force to establish a highly efficient photodynamic platform for the complete eradication of biofilms. The incorporation of a continuous, strongly electron-withdrawing PNDI network drives ultrafast cascaded ICT. This extended polymeric architecture achieves genuine spatial charge decoupling by trapping highly oxidative holes at the HOMO level for  $\cdot\text{OH}$  generation, while transporting energetic electrons over a long pathway to the peripheral molecular state for a burst of  $\cdot\text{O}_2^-$ . This potent dual-ROS mode enables an overwhelming deconstructive strike against resilient biofilms. Rather than merely inactivating the resident bacteria, R-PCDs fundamentally dismantle the robust EPS matrix by cleaving its essential eDNA, polysaccharide, and protein components. The subsequent exposure directly leads to irreversible membrane damage, dehydrogenase inactivation in the respiratory chain, and ultimate ATP depletion in both Gram-negative and Gram-positive bacteria. By eradicating the root cause of biofouling, the EPS matrix, this study not only deepens the understanding of the fundamental photophysical mechanisms underlying complex carbon nanomaterials but also provides a highly promising, light-driven, and broad-spectrum strategy for addressing the critical biofilm challenges across diverse frontier fields, ranging from clinical wound healing to large-scale marine antifouling and industrial biocorrosion mitigation.

#### Author Contributions

**Shujing Wang:** conceptualization, investigation, writing – original draft, methodology, validation, visualization, writing – review and editing, software, formal analysis, data curation. **Lei Rong:** investigation, methodology, resources, software, formal analysis, data curation. **Yanbai Chen:** investigation, methodology, resources, software. **Wenxuan He:** methodology, software. **Xiang Wen:** funding acquisition, supervision, resources. **Yi Deng:** funding acquisition, supervision, resources, software. **Shuangquan Lai:** conceptualization, investigation, funding acquisition, writing – review and editing, supervision, resources.

#### Acknowledgements

This work is jointly funded by the National Natural Science Foundation of China (22305098, 32571536, 32271392), Natural Science Foundation of Sichuan (2026NSFSC0995, 2026YFHZ0080), the Fundamental Research Funds for the Central Universities, and Sichuan University Postdoctoral Interdisciplinary Innovation Fund. The authors thank Jing Zhou (Analytical & Testing Center, SCU) for their help in CLSM. We would like to thank Dong Yu with Digital scanning system (WISLEAP WS-10), Linzhu Li with Digital scanning system (Olympus VS200) and Leica DMI 8 fluorescence microscope in Life Science Core Facilities (College of Life Sciences, SCU). The authors thank Wen Tian (Center of Engineering Experimental Teaching, School of Chemical Engineering) for their help with FTIR. The authors would like to thank Zhonghui Wang and Qingshuang Song (College of Biomass Science and Engineering, SCU) for their help in UV-vis DRS and PL spectroscopy characterizations. The authors extend their gratitude to Mr. Jian Biao from Scientific Compass ([www.shiyanjia.com](http://www.shiyanjia.com)) for providing invaluable assistance with TEM analysis. The authors would like to thank Ceshigo Research Service ([www.ceshigo.com](http://www.ceshigo.com)) for providing ESR testing.

#### Conflicts of Interest

The authors declare no conflicts of interest.

#### Data Availability Statement

The data that support the findings of this study are available from the corresponding author upon reasonable request.

#### References

1. Y. Chuang, S. Qimanguli, C. Wei, et al., “Chemically Modified and Inactivated Bacteria Enable Intra-biofilm Drug Delivery and Long-term Immunity against Implant Infections,” *Nature Biomedical Engineering* (2026), <https://doi.org/10.1038/s41551-025-01600-8>.
2. Z. Shen, S. Luo, H. Ding, et al., “Photocatalytic Activation Strategy for Sequential Prodrug Release to Overcome Resistant Biofilms,” *Journal of the American Chemical Society* 148 (2026): 11667–11682, <https://doi.org/10.1021/jacs.5c19856>.
3. G. Hou, R. Zhang, T. Zhao, et al., “Situ Biofilm Development on Microplastics and its Impact on PFAS Adsorption in Aquatic Environment,” *Water Research* 291 (2026): 125240.
4. H. Pan, X. Zhao, J. Zhao, et al., “In-situ Biofouling on Aquatic Plastics: a Potential Key Mediator of Heavy Metal Accumulation and Pathogen Association,” *Chemical Engineering Journal* 521 (2025): 166576, <https://doi.org/10.1016/j.cej.2025.166576>.
5. A. Vishwakarma, A. Narayanan, N. Kumar, et al., “Coacervate Dense Phase Displaces Surface-Established Pseudomonas aeruginosa Biofilms,” *Journal of the American Chemical Society* 146 (2024): 26397–26407, <https://doi.org/10.1021/jacs.4c09311>.
6. H. Flemming, E. D. van Hullebusch, B. J. Little, et al., “Microbial Extracellular Polymeric Substances in the Environment, Technology and Medicine,” *Nature Reviews Microbiology* 23 (2025): 87–105, <https://doi.org/10.1038/s41579-024-01098-y>.
7. L. Mathieu, I. Bertrand, Y. Abe, et al., “Drinking Water Biofilm Cohesiveness Changes under Chlorination or Hydrodynamic Stress,” *Water Research* 55 (2014): 175–184, <https://doi.org/10.1016/j.watres.2014.01.054>.
8. U. Hofer, “The Cost of Biofilms,” *Nature Reviews Microbiology* 20 (2022): 445.
9. Y. Liu, R. Chen, S. Liu, et al., “Eradicating Biofilms: Decoding Persistent Mechanisms and Combating Therapeutic Strategies,” *Advanced Healthcare Materials* 15 (2026): e02707, <https://doi.org/10.1002/adhm.202502707>.



10. H. Flemming, "Biofouling and Me: My Stockholm Syndrome With Biofilms," *Water Research* 173 (2020): 115576, <https://doi.org/10.1016/j.watres.2020.115576>.
11. X. Liu, L. Zou, B. Li, et al., "Chemical Signaling in Biofilm-mediated Biofouling," *Nature Chemical Biology* 20 (2024): 1406–1419, <https://doi.org/10.1038/s41589-024-01740-z>.
12. K. Nekouieian, M. Amiri, M. Sillanpää, F. Marken, R. Boukherroub, and S. Szunerits, "Carbon-based Quantum Particles: an Electroanalytical and Biomedical Perspective," *Chemical Society Reviews* 48 (2019): 4281–4316, <https://doi.org/10.1039/C8CS00445E>.
13. Y. Shi, Y. Zhang, Z. Wang, et al., "Onion-Like Multicolor Thermally Activated Delayed Fluorescent Carbon Quantum Dots for Efficient Electroluminescent Light-emitting Diodes," *Nature Communications* 15 (2024): 3043, <https://doi.org/10.1038/s41467-024-47372-8>.
14. Q. Chen, J. Ma, S. Yu, et al., "Small Dots, Multiple Functions": Unveiling the Veil of a Bioactive Quercetin Carbon Dot and Its Multifaceted Antibacterial and Osteogenesis Mechanisms for Infectious Bone Defect Repair," *Advanced Functional Materials* 35 (2025): 2507840, <https://doi.org/10.1002/adfm.202507840>.
15. Y. Miao, Y. Y. Nie, H. J. Zou, et al., "Carbon Dots via Synergistic Surface-Oxidation and Rigidity Enhancement With Ultra-Narrow Emission for Sensitive Near-Infrared Imaging and Sepsis Therapy," *Advanced Functional Materials* 7 (2025): e13584, <https://doi.org/10.1002/adfm.202513584>.
16. L. Ai, J. Xiao, J. Yu, et al., "Synergistic Rigidity-Enhancement and Electron-Rich Systems Engineering Robust Carbon Dots-Based Ultra-Narrowband NIR Emitters for LEDs With Superior Operational Stability," *Angewandte Chemie International Edition* 64 (2025): e202509276, <https://doi.org/10.1002/anie.202509276>.
17. Q. Jia, J. Ge, W. Liu, et al., "A Magnetofluorescent Carbon Dot Assembly as an Acidic H<sub>2</sub>O<sub>2</sub>-Driven Oxygenerator to Regulate Tumor Hypoxia for Simultaneous Bimodal Imaging and Enhanced Photodynamic Therapy," *Advanced Materials* 30 (2018): 1706090, <https://doi.org/10.1002/adma.201706090>.
18. Y. Wang, Y. Liu, H. Sun, and D. Guo, "Type I Photodynamic Therapy by Organic–inorganic Hybrid Materials: From Strategies to Applications," *Coordination Chemistry Reviews* 395 (2019): 46–62, <https://doi.org/10.1016/j.ccr.2019.05.016>.
19. B. Halliwell, "Understanding Mechanisms of Antioxidant Action in Health and Disease," *Nature Reviews Molecular Cell Biology* 25 (2024): 13–33, <https://doi.org/10.1038/s41580-023-00645-4>.
20. L. He, Q. Pan, M. Li, et al., "Amplified Copper Ion Interference and Immunomodulation Using Self-thermophoretic Nanomotors to Treat Refractory Implant-associated Biofilm Infections," *Nature Communications* 16 (2025): 9009, <https://doi.org/10.1038/s41467-025-64064-z>.
21. L. Wang, H. Fu, J. Zhao, et al., "Cascade Magnetic Hyperthermia Therapy for Biofilm Eradication and Bone Regeneration via Dual Osteoimmuno-regulation," *ACS Nano* 19 (2025): 21679–21695, <https://doi.org/10.1021/acsnano.5c04595>.
22. X. Zhang, L. Li, B. Wang, et al., "Donor-Acceptor Type Supra-Carbon-Dots With Long Lifetime Photogenerated Radicals Boosting Tumor Photodynamic Therapy," *Angewandte Chemie International Edition* 63 (2024): e202410522, <https://doi.org/10.1002/anie.202410522>.
23. D. Gao, A. Liu, Y. Zhang, et al., "Temperature Triggered High-performance Carbon Dots With Robust Solvatochromic Effect and Self-quenching-resistant Deep Red Solid state Fluorescence for Specific Lipid Droplet Imaging," *Chemical Engineering Journal* 415 (2021): 128984, <https://doi.org/10.1016/j.cej.2021.128984>.
24. C. Ji, F. Zeng, W. Xu, et al., "Hydrogen Bond-Mediated Self-Assembly of Carbon Dots Enabling Precise Tuning of Particle and Cluster Luminescence for Advanced Optoelectronic Applications," *Advanced Materials* 37 (2025): 2414450, <https://doi.org/10.1002/adma.202414450>.
25. Z. Liu, J. Li, C. Zhao, et al., "Molecular Engineering Enables Bright Carbon Dots for Super-Resolution Fluorescence Imaging and in Vivo Optogenetics," *Advanced Materials* 37 (2025): 2410786, <https://doi.org/10.1002/adma.202410786>.
26. K. J. Mintz, M. Bartoli, M. Rovere, et al., "A deep investigation into the structure of carbon dots," *Carbon* 173 (2021): 433–447.
27. S. Wang, L. Rong, W. He, Y. K. Chan, S. Lai, and Y. Deng, "Tailoring Full-Spectrum Solvatofluorochromic Carbon Dots: Deciphering Tunable Multicolor Emission Mechanisms toward Advanced Photonic Cryptography," *Nano Letters* 25 (2025): 17876–17886, <https://doi.org/10.1021/acs.nanolett.5c05189>.
28. Z. Guo, Y. Bian, L. Zhang, et al., "Multi-Stimuli-Responsive Carbon Dots With Intrinsic Photochromism and in Situ Radical Afterglow," *Advanced Materials* 36 (2024): 2409361, <https://doi.org/10.1002/adma.202409361>.
29. S. Song, L. Sui, K. Liu, et al., "Self-exothermic Reaction Driven Large-scale Synthesis of Phosphorescent Carbon Nanodots," *Nano Research* 14 (2021): 2231–2240, <https://doi.org/10.1007/s12274-020-3204-z>.
30. T. Kato, Y. Yamada, Y. Nishikawa, H. Ishikawa, and S. Sato, "Carbonization Mechanisms of Polyimide: Methodology to Analyze Carbon Materials With Nitrogen, Oxygen, Pentagons, and Heptagons," *Carbon* 178 (2021): 58–80, <https://doi.org/10.1016/j.carbon.2021.02.090>.
31. H. Ding, S. Yu, J. Wei, and H. Xiong, "Full-Color Light-Emitting Carbon Dots With a Surface-State-Controlled Luminescence Mechanism," *ACS Nano* 10 (2016): 484–491, <https://doi.org/10.1021/acsnano.5b05406>.
32. S. Zhu, J. Zhang, S. Tang, et al., "Surface Chemistry Routes to Modulate the Photoluminescence of Graphene Quantum Dots: From Fluorescence Mechanism to Up-Conversion Bioimaging Applications," *Advanced Functional Materials* 22 (2012): 4732–4740, <https://doi.org/10.1002/adfm.201201499>.
33. J. Fox, J. J. Wie, B. W. Greenland, et al., "High-strength, Healable, Supramolecular Polymer Nanocomposites," *Journal of the American Chemical Society* 134 (2012): 5362–5368, <https://doi.org/10.1021/ja300050x>.
34. S. K. M. Nalluri, C. Berdugo, N. Javid, P. W. J. M. Frederix, and R. V. Ulijn, "Biocatalytic Self-Assembly of Supramolecular Charge-Transfer Nanostructures Based on n-Type Semiconductor-Appended Peptides," *Angewandte Chemie International Edition* 53 (2014): 5882–5887, <https://doi.org/10.1002/anie.201311158>.
35. T. A. Barendt, I. Rašović, M. A. Lebedeva, et al., "Anion-Mediated Photophysical Behavior in a C60 Fullerene [3]Rotaxane Shuttle," *Journal of the American Chemical Society* 140 (2018): 1924–1936, <https://doi.org/10.1021/jacs.7b12819>.
36. G. Koshkakaryan, L. M. Klivansky, D. Cao, et al., "Alternative Donor–Acceptor Stacks From Crown Ethers and Naphthalene Diimide Derivatives: Rapid, Selective Formation From Solution and Solid State Grinding," *Journal of the American Chemical Society* 131 (2009): 2078–2079, <https://doi.org/10.1021/ja809088v>.
37. J. Li, M. Kang, Z. Zhang, et al., "Synchronously Manipulating Absorption and Extinction Coefficient of Semiconducting Polymers via Precise Dual-Acceptor Engineering for NIR-II Excited Photothermal Theranostics," *Angewandte Chemie International Edition* 62 (2023): e202301617, <https://doi.org/10.1002/anie.202301617>.
38. Y. Bi, J. Yu, J. Xiao, et al., "Visible Light Excited Time-Dependent Phosphorescence Color Tuning in Carbon Dots via Charge Transfer," *Angewandte Chemie International Edition* 64 (2025): e202506162, <https://doi.org/10.1002/anie.202506162>.
39. G. Mo, Y. Jin, Y. Deng, et al., "Band-Gap Engineering of Isoreticular Hydrogen-Bonded Organic Frameworks for Boosting Photocatalytic Hydrogen Evolution," *Angewandte Chemie International Edition* 65 (2026): e25987, <https://doi.org/10.1002/anie.202525987>.
40. S. Trasatti, "The Absolute Electrode Potential: an Explanatory Note (Recommendations 1986)," *Pure and Applied Chemistry* 58 (1986): 955–966, <https://doi.org/10.1351/pac198658070955>.
41. C. M. Cardona, W. Li, A. E. Kaifer, D. Stockdale, and G. C. Bazan, "Electrochemical Considerations for Determining Absolute Frontier



- Orbital Energy Levels of Conjugated Polymers for Solar Cell Applications,” *Advanced Materials* 23 (2011): 2367–2371, <https://doi.org/10.1002/adma.201004554>.
42. Z. Zhou, S. Zhao, Z. Li, P. Wang, S. Zhan, and M. Wang, “Activating Oxygen via the 3-Electron Pathway to Hydroxyl Radical by La–O<sub>4</sub> Single-Atom on WO<sub>3</sub> for Water Purification,” *Angewandte Chemie International Edition* 64 (2025): e202418122, <https://doi.org/10.1002/anie.202418122>.
43. M. Kim, S. U. Ryu, S. A. Park, et al., “Donor–Acceptor-Conjugated Polymer for High-Performance Organic Field-Effect Transistors: a Progress Report,” *Advanced Functional Materials* 30 (2020): 1904545, <https://doi.org/10.1002/adfm.201904545>.
44. Y. Zhang, H. Song, L. Wang, et al., “Solid-State Red Laser With a Single Longitudinal Mode From Carbon Dots,” *Angewandte Chemie International Edition* 133 (2021): 25718–25725, <https://doi.org/10.1002/ange.202111285>.
45. S. Mondal, A. Yucknovsky, K. Akulov, et al., “Efficient Photosensitizing Capabilities and Ultrafast Carrier Dynamics of Doped Carbon Dots,” *Journal of the American Chemical Society* 141 (2019): 15413–15422, <https://doi.org/10.1021/jacs.9b08071>.
46. W. Wang, J. Shao, D. Xie, et al., “Suppressing Non-Radiative Decay via Cyanation: A Promising Design Strategy for Bright Organic NIR-II Fluorophores,” 65 (2026): e22260.
47. Y. Li, X. Zhang, C. Li, et al., “Overcoming Diffusion Limit in Fenton-Like Reactions: Catalysis With Localized Dipole for Enhanced Peroxymonosulfate Activation and Targeted Pollutant Removal,” *Applied Catalysis B: Environment and Energy* 391 (2026): 126651, <https://doi.org/10.1016/j.apcatb.2026.126651>.
48. Q. Wang, Q. Cheng, B. Wang, et al., “From Exciton Dynamics to Cell Fate: a Carbon Dot Based NIR Photocatalytic Platform for Pyroptosis via Self-Trapped Excitons,” *Advanced Functional Materials* 35 (2025): e10756, <https://doi.org/10.1002/adfm.202510756>.
49. Y. Cao, Y. Li, A. Du, Y. Zhang, and W. Xie, “Unlocking Plasmonic Hot Electron Utilization on Palladium Nanoparticles via Modulation of the Bimetallic Interface for Enhanced Photocatalysis,” *Journal of the American Chemical Society* 148 (2026): 893–901, <https://doi.org/10.1021/jacs.5c16605>.
50. X. Zhang, L. Yang, M. Jia, et al., “Charge-Transfer-Coupled J-Aggregation Enhances ROS Generation via Efficient Intermolecular Electron Transfer for Photodynamic Therapy,” *Advanced Materials* 38 (2026): e13693, <https://doi.org/10.1002/adma.202513693>.
51. A. Kong, Y. Chen, Y. Zou, et al., “Coordination Orientation Isomerism Boosting Concerted Hydrogen Peroxide Photosynthesis,” *Nature Communications* (2026), <https://doi.org/10.1038/s41467-026-72809-7>.
52. R. Chen, F. Fan, and C. Li, “Unraveling Charge-Separation Mechanisms in Photocatalyst Particles by Spatially Resolved Surface Photovoltage Techniques,” *Angewandte Chemie International Edition* 61 (2022): e202117567, <https://doi.org/10.1002/anie.202117567>.
53. R. Wu, K. Sun, G. Shi, et al., “Construction of Weakly Hybridized Excited State Using Donor- $\pi$ -Acceptor Structure and Applications: From Highly Efficient Pure-Blue Electro-Fluorescence to Visible-Light Polymerization,” *Advanced Functional Materials* 34 (2024): 2403501.
54. L. Zhu, G. Song, W. Zhang, et al., “Aggregation Induced Emission Luminescent Bacteria Hybrid Bionic Robot for Multimodal Phototheranostics and Immunotherapy,” *Nature Communications* 16 (2025): 2578, <https://doi.org/10.1038/s41467-025-57533-y>.
55. H. Xu, M. Zheng, D. Ye, et al., “Ultrasound-Triggered Activation of p-Azidobenzyloxycarbonyl-Based Prodrugs via Radical-Mediated Cascade Elimination,” *Journal of the American Chemical Society* 147 (2025): 20667–20679, <https://doi.org/10.1021/jacs.5c03878>.
56. X. Wang, X. Sun, Y. Zeng, S. Liu, Q. Yi, and Y. Wu, “Membrane Fusion Strategy Boosts Immune Homeostasis, Mobilizing Macrophages to Eliminate Bacteria and Accelerate Skin Regeneration in Infected Burn Wound,” *Advanced Functional Materials* 35 (2025): 2416791, <https://doi.org/10.1002/adfm.202416791>.
57. S. Lai, B. Cao, X. Ouyang, et al., “Fluorescent Microneedle-Based Theranostic Patch for Naked-Eye Monitoring and on-Demand Phototherapy of Bacterial Biofilm Infections,” *Advanced Functional Materials* 35 (2025): 2415559, <https://doi.org/10.1002/adfm.202415559>.

### Supporting Information

Additional supporting information can be found online in the Supporting Information section.

**Supporting File:** anie72993-sup-0001-SuppMat.docx.